

# Physical Properties of UDF12 Galaxies in Cosmological simulations

Ikkoh Shimizu<sup>1,2\*</sup>, Akio K. Inoue<sup>1</sup>, Takashi Okamoto<sup>3</sup> and Naoki Yoshida<sup>4,5</sup>

<sup>1</sup>College of General Education, Osaka Sangyo University, 3-1-1 Nakagaito, Daito, Osaka 574-8530, Japan

<sup>2</sup>Department of Astronomy, School of Science, The University of Tokyo, 7-3-1 Hongo, Bunkyo-ku, Tokyo 113-0033

<sup>3</sup>Department of CosmoSciences Graduate School of Science, Hokkaido University, N10 W8, Kitaku, Sapporo, 060-0810, Japan

<sup>4</sup>Department of Physics, The University of Tokyo, 7-3-1 Hongo, Bunkyo-ku, Tokyo 113-0033, Japan

<sup>5</sup>Kavli Institute for the Physics and Mathematics of the Universe, TODIAS, The University of Tokyo, 5-1-5 Kashiwanoha, Kashiwa, Chiba 277-8583, Japan

In original form 2013 May 7

## ABSTRACT

We have performed a large cosmological hydrodynamics simulation tailored to the deep survey with the Hubble Space Telescope made in 2012, the so-called UDF12 campaign. After making a light-cone output, we have applied the same color selection criteria as the UDF12 campaign to select galaxies from our simulation, and then, have examined the physical properties of them as a proxy of the real observed UDF12 galaxies at  $z > 7$ . As a result, we find that the halo mass is almost linearly proportional to the observed ultraviolet (UV) luminosity ( $4 \times 10^{11} M_{\odot}$  at  $M_{UV} = -21$ ). The dust attenuation and UV slope  $\beta$  well correlates with the observed UV luminosity, which is consistent with observations quantitatively. The star formation rate (SFR) is also linearly proportional to the stellar mass and the specific SFR shows only a weak dependency on the mass. We also find an increasing star formation history with a time-scale of  $\sim 100$  Myr in the high- $z$  galaxies. An average metallicity weighted by the Lyman continuum luminosity reaches up to  $> 0.1$  Solar even at  $z \sim 10$ , suggesting a rapid metal enrichment. We also expect  $\geq 0.1$  mJy at 350 GHz of the dust thermal emission from the galaxies with  $H_{160} \leq 27$ , which can be detectable with the Atacama Large Millimetre-submillimetre Array. The galaxies selected by the UDF12 survey contribute to only 52–12% of the cosmic SFR density from  $z \sim 7$  to  $z \sim 10$ , respectively. The James Webb Space Telescope will push the detection fraction up to 77–72%.

**Key words:** cosmology – observations; galaxies – evolution; galaxies – formation; galaxies – high-redshift; galaxies – luminosity function, mass function;

## 1 INTRODUCTION

Structure formation in the Universe proceeds from a small scale to a large scale through accretion and merging processes of dark matter halos in the context of the current concordance  $\Lambda$  cold dark matter ( $\Lambda$ CDM) cosmology. Yet baryonic processes making luminous objects such as galaxies are not well understood and this is one of the most important questions in the modern observational cosmology. In order to understand the processes of galaxy formation and evolution, it is important to look into the site where galaxies are forming in the very high- $z$  Universe. They are intriguing objects as the potential sources causing the cosmic reionization which is also one of the hottest topics in the current cosmology research.

High- $z$  galaxy candidates upto  $z \sim 7$  have been detected by ground-based large telescopes (Ota et al. 2008; Ouchi et al. 2009, 2010; Castellano et al. 2010; Bowler et al. 2012). The redshifts of some of the galaxies are confirmed by spectroscopy (Vanzella et al. 2011; Ono et al. 2012; Shibuya et al. 2012; Finkelstein et al. 2013). However, it is difficult to detect galaxies at  $z > 7$  using the dropout (Lyman break) method by the ground-based telescopes because the Ly $\alpha$  break shifts to the near-infrared (NIR) wavelength where the observation is strongly affected by the Earth’s atmosphere. Therefore, a space telescope which is free from the atmospheric effect is needed to detect highest- $z$  galaxies (Yan & Windhorst 2004; Bouwens et al. 2004). Since the new Wide Field Camera (WFC3) was installed on the Hubble Space Telescope (HST) in 2009, its NIR channel has revolutionized the search for highest- $z$  galaxies (Oesch et al. 2010; McLure et al. 2010; Wilkins et al.

\* E-mail: shimizu@astron.s.u-tokyo.ac.jp

2010; Labbé et al. 2010; Bouwens et al. 2010, 2011). In 2012, a new campaign to take the deepest images of the sky ever obtained was conducted with HST/WFC3 (Ellis et al. 2013; McLure et al. 2013; Schenker et al. 2013; Dunlop et al. 2013; Robertson et al. 2013; Ono et al. 2013; Koekemoer et al. 2013; Oesch et al. 2013). This is called the UDF12 campaign. A number of candidates of galaxies beyond  $z = 7$  have been discovered in the UDF12 data (Ellis et al. 2013; McLure et al. 2013; Schenker et al. 2013; Oesch et al. 2013). The data set is the best one to investigate such highest- $z$  galaxies even though their redshifts have not been confirmed by spectroscopy yet (see Inoue et al. (2014) about a spectroscopic follow-up strategy with ALMA).

In order to study the physical properties of high- $z$  galaxies, the so-called spectral energy distribution (SED) fitting is often used (Sawicki & Yee 1998). When applying the method to the UDF12 galaxies, however, the narrow coverage of the SEDs causes a problem. The HST/WFC3 data, in fact, cover only a narrow range of ultraviolet (UV) in the rest-frame of the galaxies. The galaxies at very high-redshifts are detected only one longest wavelength band at about  $1.6 \mu\text{m}$  in the observer’s frame. Spitzer/IRAC data sometimes help the situation for brightest galaxies, but it is limited because of shallowness of the IRAC data.

In the preset paper, we examine the physical properties of the UDF12 galaxies by utilizing a cosmological hydrodynamics simulation in order to overcome the limitation of the narrow coverage of the SEDs with observational data currently available for highest- $z$  galaxies. Galaxy formation models based on cosmological hydrodynamics simulations are now well developed and can reproduce reasonably well statistical quantities such as luminosity functions (LFs), stellar mass functions (SMFs), and cosmic star formation history (e.g., Nagamine et al. 2010; Salvaterra et al. 2011, 2013; Shimizu, Yoshida & Okamoto 2011, 2012; Jaacks et al. 2012a,b, 2013; Biffi & Maio 2013; Dayal et al. 2013). In such a simulation, one can select simulated galaxies which would be detected by the UDF12 campaign and would satisfy the color selection criteria. Then, we can investigate the physical properties such as halo mass, stellar mass, star formation rate of the selected “mock-UDF12 galaxies”. A similar approach has been proposed by Overzier et al. (2013) but their method is based on a semi-analytic model of galaxy formation and did not discuss the highest- $z$  galaxies sampled by the UDF12 campaign.

In section 2, we describe our numerical simulations and calibration parameters. Then, we virtually observe the galaxies produced by our simulation through a light-cone output and select simulated galaxies by the same criteria as those in the UDF12 survey in section 3. In section 4, we present physical properties of the selected mock-UDF12 galaxies in our simulation. In section 5, we discuss a few implications and predictions. The final section is devoted for our conclusion.

Throughout this paper, we adopt a  $\Lambda$ CDM cosmology with the matter density  $\Omega_M = 0.27$ , the cosmological constant  $\Omega_\Lambda = 0.73$ , the Hubble constant  $h = 0.7$  in the unit of  $H_0 = 100 \text{ km s}^{-1} \text{ Mpc}^{-1}$  and the baryon density  $\Omega_B = 0.046$ . The matter density fluctuations are normalised by setting  $\sigma_8 = 0.81$  (Komatsu et al. 2011). All magnitudes are quoted in the AB system (Oke 1990). The assumed initial mass function (IMF) in the observational data and in

our simulation is always the Salpeter IMF with the mass range of  $0.1\text{--}100 M_\odot$ .

## 2 COSMOLOGICAL SIMULATIONS

We first describe our cosmological hydrodynamics simulation. We calibrate parameters in the code by comparing the SMF observed at  $z = 7$ . Then, we introduce the SED model of the simulated galaxies. To do this, we need to adopt a recipe for the dust attenuation which has additional parameters. To calibrate them, we compare the UV LFs in our simulation with the observed ones at  $z = 7, 8, 9$  and  $z = 10$ . These observational data are compiled from literatures including the UDF12 results.

Our simulation code is based on an updated version of the Tree-PM smoothed particle hydrodynamics (SPH) code GADGET-3 which is a successor of Tree-PM SPH code GADGET-2 (Springel 2005). We have implemented relevant physical processes such as star formation, supernova (SN) feedback and chemical enrichment following Okamoto, Nemmen & Bower (2008); Okamoto, & Frenk (2009); Okamoto et al. (2010). As introduced by Okamoto et al. (2010), we have assumed that the initial wind speed of gas around stellar particles in which SNe occur is proportional to the local velocity dispersion of dark matter. The feedback model is motivated by recent observations of Martin (2005).

We employ a total of  $2 \times 640^3$  particles for dark matter and gas in a comoving volume of  $50h^{-1} \text{ Mpc}$  cube. The mass of a dark matter particle is  $3.01 \times 10^7 h^{-1} M_\odot$  and that of a gas particle is initially  $6.09 \times 10^6 h^{-1} M_\odot$ , respectively. The softening length for the gravitational force is set to be  $3 h^{-1} \text{ kpc}$  in comoving unit. Gas particles can spawn star particles when they satisfies a set of standard criteria for star formation, and then, their mass is reduced. On the other hand, their mass increases when the stellar population evolve and return a part of the mass including metal elements into the interstellar medium. A star particle represents a cluster of stars with a range of stellar masses because individual stars can not be resolved in the cosmological hydrodynamic simulation. For each snapshot of the simulation, we run a friends-of-friends (FoF) group finder with a comoving linking length of 0.2 in units of the mean particle separation to identify groups of dark matter particles as halos. Gas and star particles near dark matter particles which compose a FoF group are also regarded as the member of the group. Then, we identify gravitationally bound groups of at least 32 total (dark matter+gas+star) particles as substructures (subhalos) in each FoF group using SUBFIND algorithm developed by Springel et al. (2001). We regard substructures that contain at least 5 star particles as bona-fide galaxies. Above this threshold of the star particle number, the discreteness of the stellar mass begins to disappear. We note that the minimum halo mass of our simulated galaxies is around  $10^9 M_\odot$  which depends on the relative fraction of dark matter, gas and star particles. The minimum stellar mass of our simulated galaxies is around  $10^7 M_\odot$  which depends on the age of individual star particle in galaxies. Henceforth, we only use galaxies satisfying these conditions for our study. This treatment of the simulated galaxies is different from our previous work

(Shimizu, Yoshida & Okamoto 2011, 2012) and thus affects the shape of the stellar mass function at lower- $z$  because the FoF halos may contain many substructures. However, the overall effect is not significant at higher- $z$  where we discuss in this paper. Some recent theoretical work claims that the effect of the so-called chemical feedback (i.e., the transition from PopIII to PopII/PopI stars) that affects the early evolution of very high- $z$  galaxies and in particular their metal enrichment history (e.g., Salvaterra et al. 2011, 2013; Dayal et al. 2013). In this study, however, we do not consider this effect (i.e., we consider only PopII/PopI star population) because our simulation resolution is not enough to discuss the effect.

In order to calibrate parameters in the code such as SN feedback efficiency, we compare our model with observations of the stellar mass function (SMF) of galaxies, assuming the observed SMFs to be complete and correct. Fig. 1 represents our SMF at  $z = 7$  (left panel) and those at  $z = 7$  to  $z = 10$  (right panel). In the left panel, we also plot the observational results (the points with error bars) at  $z = 7$  taken from González et al. (2011). Our model reproduce the observed SMF reasonably well. There is an issue of the definition of the stellar mass for low- $z$  galaxies: the mass including remnant mass or not (Shimizu & Inoue 2013). However, the effect is negligible at the high- $z$ .

When comparing our simulated galaxies with observed galaxies, we calculate the spectral energy distribution (SED) of the simulated galaxies. The SED of each star particle which has its own age, metallicity, and mass is calculated by using the population synthesis code PÉGASE (Fioc & Rocca-Volmerange 1997). We assume a universal Salpeter initial mass function (IMF) with mass range  $0.1 M_{\odot}$  to  $100 M_{\odot}$  for all star particles. We then sum the SEDs of individual star particles composing a simulated galaxy to obtain the total intrinsic SED of the galaxy. Schaerer & de Barros (2008) argued that nebular components (continuum + line) affect the rest-frame optical band magnitude for high- $z$  galaxies. In this study, however, we consider only the UV range  $< 2000 \text{ \AA}$ , where Ly $\alpha$  emission line is the only important nebular line. Some spectroscopic surveys of Ly $\alpha$  emission line at  $z > 8$  have been performed, but all failed (Brammer et al. 2013; Bunker et al. 2013; Capak et al. 2013; Treu et al. 2013), probably because of heavy absorption by intergalactic neutral hydrogen before the completion of the cosmic reionization. The nebular continuum does not contribute to the SEDs in the UV range if the age of galaxies is larger than 50 Myr (Inoue 2011a). Thus, we do not consider the contribution of nebular components in this study.

We treat the dust attenuation similarly to Shimizu, Yoshida & Okamoto (2011) and Shimizu, Yoshida & Okamoto (2012). An important difference is that, in this study, we simply adopt the Calzetti law (Calzetti et al. 2000) rather than using  $Q$  values of a specific material and size. The optical depth  $\tau_d$  at  $1500 \text{ \AA}$ , which is used for the normalization of the attenuation law, is calculated by the following equation:

$$\tau_d = \frac{3\Sigma_d}{4a_d s}, \quad (1)$$

where  $a_d$  and  $s$  are a typical size and the material density of dust grains, respectively. We set  $a_d = 0.1 \mu\text{m}$  and

$s = 2.5 \text{ g cm}^{-3}$  following SNe dust production models (Todini & Ferrara 2001; Nozawa et al. 2003). Note that any effects of different choices of these values are absorbed in one parameter determining the dust surface mass density,  $\Sigma_d$ , as described below. The surface density is defined by the following equation:

$$\Sigma_d = \frac{M_d}{\pi r_d^2}, \quad (2)$$

where  $M_d$  and  $r_d$  are the total dust mass and the effective radius of the dust distribution in a galaxy, respectively. We assume  $M_d$  and  $r_d$  to be proportional to the metal mass,  $M_{\text{metal}}$ , and the half mass radius,  $r_{\text{half}}$ , of the dark matter distribution in a galaxy, respectively. The latter two values are directly calculated in our simulation. Therefore,  $M_d$  and  $r_d$  are expressed as  $e_{M_d} M_{\text{metal}}$  and  $e_{r_d} r_{\text{half}}$ , respectively, where  $e_{M_d}$  and  $e_{r_d}$  are the proportional constants of the dust mass and the effective radius, respectively. These two parameters, in fact, can be reduced to one parameter. Equation (2) is reduced to

$$\Sigma_d = e_{\tau} \frac{M_{\text{metal}}}{\pi r_{\text{half}}^2}, \quad (3)$$

where  $e_{\tau} = e_{M_d}/e_{r_d}^2$ , which is a global constant for all the galaxies in our simulation. Then, we calculate the escape probability of UV photons at  $1500 \text{ \AA}$  ( $f_{\text{UV}}$ ) using the following equation:

$$f_{\text{UV}} = \frac{1 - \delta}{2}(1 + e^{-\tau_d}) + \frac{\delta}{\tau_d}(1 - e^{-\tau_d}), \quad (4)$$

where  $\delta$  is a parameter whose value is ranging from 0 to 1. In Equation (4), a uniform slab where stars and dust are well mixed is sandwiched in the middle of two stellar layers, where dust is negligible (Xu & Buat 1995). The parameter  $\delta$  is the fraction of the thickness of the central star+dust slab in the total thickness; it is the well-mixed dusty slab geometry when  $\delta$  is unity, and it is the case with a central infinitely thin dusty sheet when  $\delta$  is zero. Such a sandwich geometry is favored to explain the observed relation between the UV color and the infrared-to-UV flux ratio of nearby galaxies (Inoue et al. 2006). In addition, we have found a similar situation in our simulation: star particles are sometimes found at the periphery of subhalos and the dust (or gas) density at such region is very low. The escape probability  $f_{\text{UV}}$  is saturated at  $(1 - \delta)/2$  when  $\tau_d \rightarrow \infty$ .

We calibrate  $e_{\tau}$  and  $\delta$  so as to reproduce the observed UV luminosity function (LF) at  $z = 7$ , and we keep these values even at higher redshifts. For the cosmological simulation in this study, we adopt  $e_{\tau} = 3.7$  and  $\delta = 0.65$ , respectively. If we set  $e_{M_d} = 0.5$ , with which we can reproduce the number count of the submm galaxies (Shimizu, Yoshida & Okamoto 2012),  $e_{r_d}$  is uniquely determined as  $e_{r_d} = 0.36$ . Interestingly, this value results in the dust distribution radius,  $r_d$ , very similar to the half-mass radius of the stellar mass distribution. We also apply the IGM absorption for the blue side of  $1216 \text{ \AA}$  following Madau (1995) with an extrapolation for  $z > 7$ , which should not cause a significant uncertainty because the spectrum below Ly $\alpha$  is completely damped by the IGM absorption for such high-redshifts.

Since our simulation box size has the angular size of about  $25'$  at  $z = 7-10$ , we can have about 130 HST/WFC3 fields-of-view in one side of the box. Then, we calculate the UV LFs in the 130 rectangular parallelepiped sub-boxes

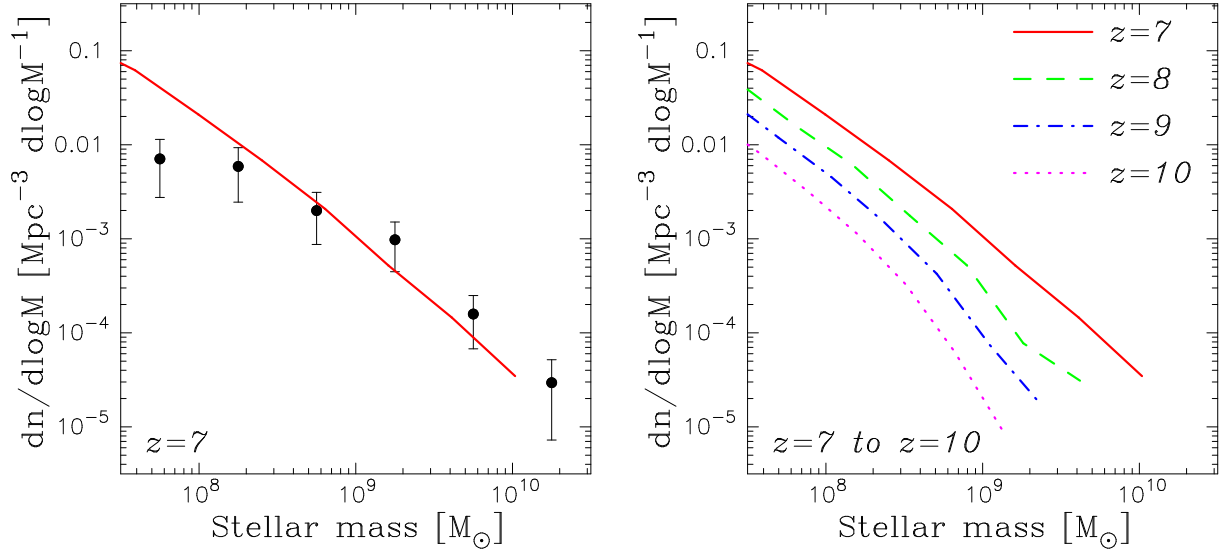


**Figure 1.** The stellar mass functions (SMF) at  $z = 7$  (left panel) and higher (right panel). The solid, dashed, dash-dotted and dotted lines show the SMFs at  $z = 7, 8, 9$  and  $z = 10$ , respectively. For  $z = 7$ , we also plot observational data as the points with error bars taken from González et al. (2011) in the left panel.

which has the approximately UDF12-sized area in one side. Figure 2 shows the average of the UV LFs (solid lines) and their standard deviations (shaded areas) of our simulation results at  $z = 7, 8, 9$  and  $z = 10$ . The points with error-bars represent a compilation of several observational results (Robertson et al. 2010; Bouwens et al. 2011; Bradley et al. 2012; Oesch et al. 2012; McLure et al. 2013; Oesch et al. 2013; Schenker et al. 2013). Our models reproduce the observed LFs reasonably well within the standard deviations which express the cosmic variance of the UDF12-sized pencil beam survey. We also show the average UV LFs for the case without dust attenuation as the dashed lines, indicating a certain amount of dust attenuation even at  $z > 7$ .

### 3 MOCK OBSERVATION

We need to select galaxies which would be detected and selected in the UDF12 campaign. The construction of the mock-UDF12 sample is important for this study. It should be close similarly to the real observation. First, we make a light-cone output from a number of snapshots of the simulation. Then, we apply the same color selection criteria as for the real UDF12 galaxies.

In general, the survey depth along the line-of-sight is very wide of the Lyman break method using broad-band filters. Thus, we can not cover all the survey volume by one snapshot of our simulation. In order to directly compare our model with such observations, we generate a light-cone output which extends from  $z = 6$  to  $z = 12$  using a number of simulation outputs. We coordinate the output redshifts to fill the volume of a light-cone from  $z = 6$  to  $z = 12$  without any gap. We then randomly shift and rotate each simulation box so that the same objects do not appear multiple times on a single line-of-sight at different epochs.

In order to directly compare our model with observations, we calculate broad-band magnitudes of the simulated galaxies on the light-cone and choose dropout galaxies with

the same manner of the observations. We use the same set of broad-band filters as the UDF12 which has WFC3/IR ( $Y_{105}, J_{125}, JH_{140}$  and  $H_{160}$ ) and ACS ( $B_{435}, V_{606}, i_{775}, I_{814}$  and  $z_{850}$ ) filters. We first apply the detection limit of the UDF12 survey. The conditions are  $Y_{105} \leq 30$  and  $J_{125} \leq 30$  for the  $z \sim 7$  selection,  $J_{125} \leq 30$  and  $H_{160} \leq 30$  for the  $z \sim 8$  selection and  $JH_{140} \leq 30$  and  $H_{160} \leq 30$  for the  $z \sim 9$  and the  $z \sim 10$  selections, respectively. Then, we apply the color selection criteria for  $z \sim 7$  as

$$\begin{aligned} z_{850} - Y_{105} &> 0.7 \\ Y_{105} - J_{125} &< 0.4, \end{aligned} \quad (5)$$

and for  $z \sim 8$  as

$$\begin{aligned} Y_{105} - J_{125} &> 0.5 \\ J_{125} - H_{160} &< 0.4, \end{aligned} \quad (6)$$

as in Schenker et al. (2013). The color selection criteria for  $z \sim 9$  are

$$\begin{aligned} (Y_{105} + J_{125})/2 - JH_{140} &> 0.75 \\ (Y_{105} + J_{125})/2 - JH_{140} &> 0.75 + 1.3 \times (JH_{140} - H_{160}) \end{aligned} \quad (7)$$

and for  $z \sim 10$  are

$$\begin{aligned} J_{125} - H_{160} &> 1.2 \\ JH_{140} - H_{160} &< 1.0, \end{aligned} \quad (8)$$

as in Oesch et al. (2013). Note that we consider no effect occurring in real observations such as observational noise, surface brightness dimming, object detection incompleteness, etc., in the selection procedure. Therefore, we have assumed these effects to be small. We reserve to examine these effects in future work.

Fig. 3 shows the spacial distribution of the color selected simulated galaxies. The red, green, blue and magenta points represent the simulated galaxies selected by the criteria for  $z \sim 7, 8, 9$  and  $z \sim 10$ , respectively. The brown points are

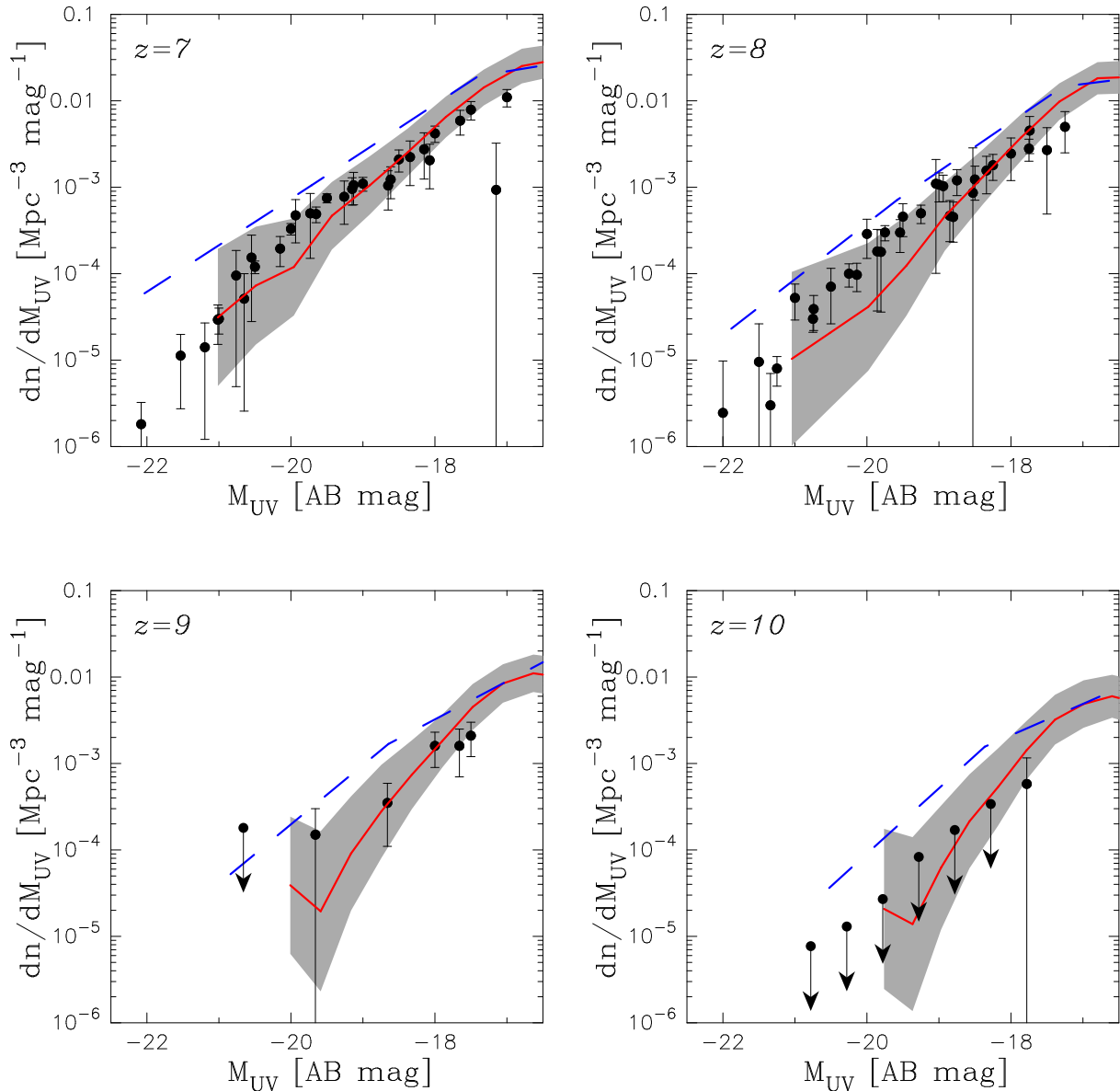


**Figure 2.** The UV luminosity functions (LFs) from  $z = 7$  to  $z = 10$ . The solid lines and dashed lines are the UV LFs with and without the dust attenuation, respectively, averaged over the entire box of our simulation. The shaded regions show the effect of the cosmic variance for a number of the UDF12-sized surveys taken from the simulation box in the case with the dust attenuation. The points with error-bars or arrows are shown the observational data (Robertson et al. 2010; Bouwens et al. 2011; Bradley et al. 2012; Oesch et al. 2012; McLure et al. 2013; Oesch et al. 2013; Schenker et al. 2013).

the galaxies doubly selected by the criteria for  $z \sim 8$  and  $z \sim 9$ . The point size represents  $H_{160}$  band magnitude and the largest (smallest) one corresponds to  $H_{160} = 25$  ( $H_{160} = 30$ ). We note that almost all simulated galaxies selected by the criteria of  $z \sim 10$  are also selected by the criteria of  $z \sim 9$ . We find that only a small number of galaxies are selected at  $z > 10$  in our simulation.

We also check the selection efficiency of the color selections. Fig. 4 presents the number fraction of galaxies brighter than the observational limiting magnitude of 30 mag and satisfying the color criteria among all the galaxies in our simulation (see sec.2 for the definition of the galaxies) as a function of redshift. The solid, dashed, dash-dotted and dotted lines are the fractions for  $z \sim 7$ , 8, 9 and  $z \sim 10$  selections,

respectively. The redshift ranges selected are  $6.2 \leq z \leq 7.2$  ( $z \sim 7$  color selection),  $7.1 \leq z \leq 8.8$  ( $z \sim 8$  color selection),  $8.0 \leq z \leq 10.8$  ( $z \sim 9$  color selection) and  $9.5 \leq z \leq 10.6$  ( $z \sim 10$  color selection). We find that the color selection works reasonably well. Next, we note a remarkably small number fraction of the galaxies selected as mock-UDF12 galaxies from all galaxies in our simulation. Interestingly, the number fraction of the color selected galaxies is less than 13% even at  $z \sim 7$  and less than 3% at  $z \sim 10$ . This means that the galaxies detected in the current deepest survey are still just the tip of iceberg and we probably miss almost all star forming galaxies at  $z > 7$ . We revisit this issue later in section 5.3.

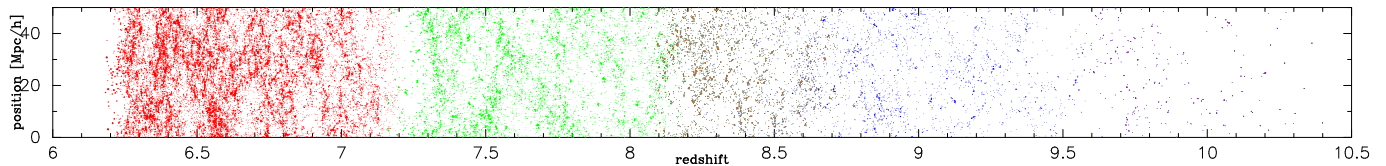


**Figure 3.** The spatial distribution of the simulated galaxies satisfying at least one color selection criterion. The red, green, blue and magenta points represent the galaxies selected by the criteria for  $z \sim 7, 8, 9$  and  $10$ , respectively. The brown points are the galaxies selected by both criteria for  $z \sim 8$  and  $9$ . The point size represents  $H_{160}$  band magnitude from  $H_{160} = 25$  to  $30$  mag which is the detection limit of the UDF12 survey.

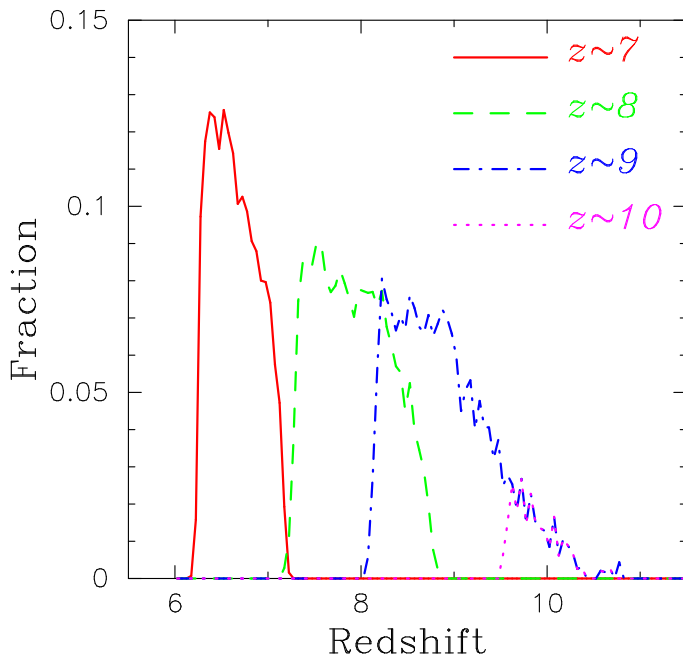


**Figure 4.** The number fraction of galaxies brighter than the observational limiting magnitude of  $30$  mag and satisfying the color criteria among all the galaxies resolved in our simulation as a function of redshift. The solid, dashed, dash-dotted and dotted lines are the fraction for  $z \sim 7, 8, 9$  and  $z \sim 10$  selections, respectively. The redshift ranges of galaxies selected are  $6.2 \leq z \leq 7.2$  ( $z \sim 7$  color selection),  $7.1 \leq z \leq 8.8$  ( $z \sim 8$  color selection),  $8.0 \leq z \leq 10.8$  ( $z \sim 9$  color selection) and  $9.5 \leq z \leq 10.6$  ( $z \sim 10$  color selection), respectively.

## 4 RESULTS

We have constructed a mock-UDF12 galaxy sample from our simulation in the previous section and we are now ready to examine their physical properties. First, we examine the halo and stellar masses of the mock-UDF12 galaxies. Second, the dust attenuation and UV slope of the mock-UDF12 galaxies are discussed. Third, we look into the correlation between the stellar mass and star formation rate (SFR) and specific SFR. We also check the cosmic SFR density at  $z > 7$ . Then, the ages and the star formation history of the galaxies are examined. Finally, the metallicity, morphology and size are investigated.

### 4.1 Halo Mass and Stellar Mass

In this subsection, we study the relation between the UV magnitude and the halo or stellar mass. The left and right

panels in Fig. 5 represent the halo masses and the stellar masses of the mock-UDF12 galaxies, respectively, as a function of the absolute UV magnitude calculated with the dust attenuation. Hereafter, we denote the absolute UV magnitude with the dust attenuation as just the absolute UV magnitude or the UV magnitude. The small triangle, square, circle and star points represent the each mock-UDF12 galaxy at  $z \sim 7, 8, 9$  and  $z \sim 10$ , respectively. The large points with error-bars are the median values and the central 68% ranges in halo mass bins. Interestingly, the relation between the halo or stellar mass and the UV magnitude is not significantly different for different redshifts. This indicates that the mass–luminosity relation for the mock-UDF12 galaxies is independent of the redshift and the mass–luminosity ratio in a certain halo mass at different epoch is almost constant. We here present simple formulae to estimate the halo or stellar mass from the UV magnitude. Let us assume a functional form as  $a \times 10^{b \times M_{UV}}$  where  $a$  and  $b$  are the fitting parameters. If  $b$  is equal to  $-0.4$ , then the UV luminosity is linearly proportional to the host halo (or stellar) mass. For the mock-UDF12 galaxies, we have obtained

$$\frac{M_{\text{halo}}}{M_{\odot}} = 278 \times 10^{-0.44 M_{UV}}, \quad (9)$$

for the halo mass relation and

$$\frac{M_{*}}{M_{\odot}} = 0.0071 \times 10^{-0.58 M_{UV}}, \quad (10)$$

for the stellar mass relation. Therefore, the UV luminosity is almost linearly proportional to the halo mass for the mock-UDF12 galaxies, but the stellar mass scales more strongly with the magnitude. Using Equation (9) and (10), we have obtained

$$\frac{M_{*}}{M_{\text{halo}}} = 0.012 \left( \frac{M_{\text{halo}}}{10^{11} M_{\odot}} \right)^{0.31}, \quad (11)$$

for the relation between the halo mass and the stellar mass when the halo mass is less than  $10^{12} M_{\odot}$ . Interestingly, this is similar to the results at  $z = 7$  and  $8$  of Behroozi et al. (2013) in which they have performed a multi-epoch abundance matching method.

### 4.2 Dust Attenuation

According to Dunlop et al. (2013), the UDF12 galaxies at  $z \geq 7$  are little affected by dust. However, as already shown in Fig. 2, we need a certain amount of dust attenuation to reproduce the observed UV LFs. Let us compare the dust attenuation in the mock-UDF12 galaxies with the observations to test whether our treatment for the dust attenuation works well quantitatively.

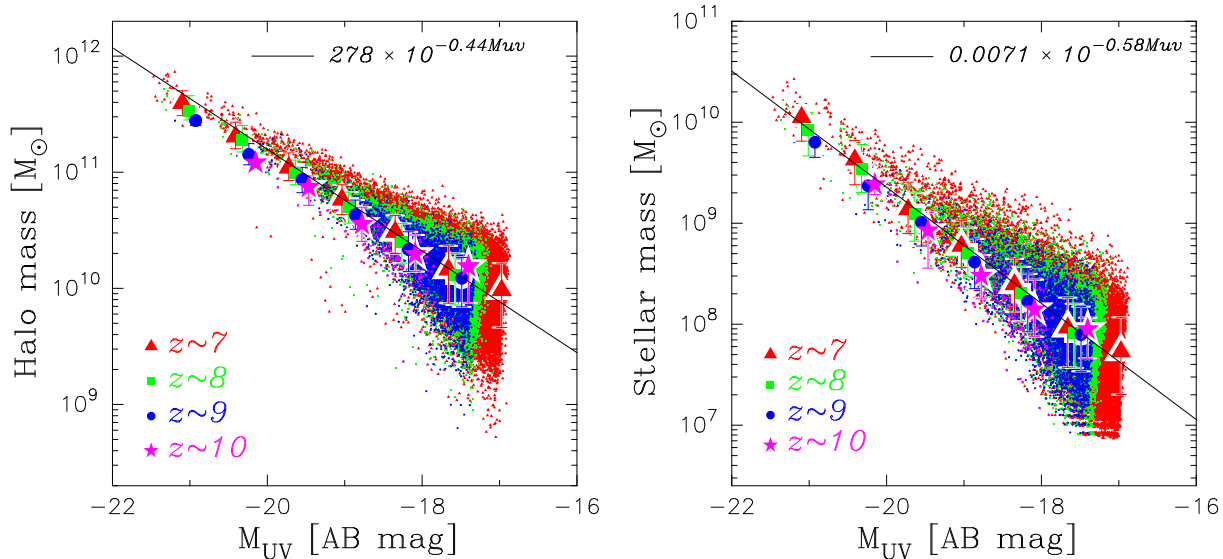


**Figure 5.** The halo mass (left panel) and the stellar mass (right panel) as a function of the ‘observed’ absolute UV magnitude calculated directly from the observable magnitude without any correction for dust attenuation. The small triangle, square, circle and star points represent the mock-UDF12 galaxies at  $z \sim 7$ , 8, 9 and  $z \sim 10$ , respectively. The large points with error-bars are the median values and the central 68% ranges in halo mass bins. The solid lines show the fitting functions and the formulae are noted in the panels.

The top left panel of Fig. 6 represents the dust attenuation  $A_{UV}$  at  $1500 \text{ \AA}$  as a function of the UV magnitude. The small points are the UV attenuation of each simulated galaxy, while the large points with error-bars are the median values and the central 68% ranges in UV magnitude bins. The range of the dust attenuation is  $A_{UV} = 0$  to  $A_{UV} = 1.9$ . This upper limit of  $A_{UV}$  comes from our recipe of the UV escape probability described in equation (4); we have a lower limit of the probability as  $(1 - \delta)/2$  when  $\tau_d \rightarrow \infty$  and we set  $\delta = 0.65$ . The  $A_{UV}$  range corresponds to  $A_V = 0 - 0.76$  under the Calzetti law we assumed (i.e.,  $A_{1500 \text{ \AA}}/A_{5500 \text{ \AA}} = 2.5$ ). Interestingly, the typical value of the dust attenuation is proportional to the UV magnitude. We also find that there are no luminous ( $M_{UV} \leq -21$ ) galaxies with less attenuation ( $A_{UV} \leq 1.5$ ) but faint galaxies are distributed over all the range of  $A_{UV}$ . Dunlop et al. (2013) argue  $A_V \sim 0.2$  for the UDF12 galaxies with the Calzetti law, which corresponds to  $A_{UV} \sim 0.5$ . A similar attenuation is found for  $M_{UV} = -18$  mock-UDF12 galaxies, whereas a larger attenuation is found for more UV luminous galaxies. Recently, Kimm & Cen (2013) argue a possibility of  $A_V \sim 1.8$  which is more than a factor of 2 larger than our result. We also find that the dust attenuation is not zero even in galaxies observed at  $z \sim 10$  in our simulation. Note that we have solved the chemical evolution (i.e., dust amount evolution) consistently with the star formation activity in galaxies in our simulation although we have assumed a constant dust-to-metal ratio which may evolve depending on the star formation history (Inoue 2011b, 2003).

Next we explore the UV slope. In order to compare our simulations with the observation, we adopt exactly the same formulae as Dunlop et al. (2013) to calculate the UV slope  $\beta$ :

$$\beta = 4.43(J_{125} - H_{160}) - 2, \quad (12)$$

for  $z \sim 7$  and  $z \sim 8$  galaxies, and

$$\beta = 9.32(JH_{140} - H_{160}) - 2, \quad (13)$$

for  $z > 8.5$  galaxies. The top right, the bottom left and the bottom right panels show the UV slope  $\beta$  for the mock-UDF12 galaxies at  $z \sim 7$ , 8 and  $z \sim 9$ , respectively. The small points are the UV slope  $\beta$  of each simulated galaxy, while the large points with error-bars are the median values and the central 68% ranges in UV magnitude bins. We also plot the observed UV slope  $\beta$  (cross points) taken from Dunlop et al. (2013). The uncertainty on  $\beta$  for each measurement reaches 1.2 for  $z \sim 7$  and  $\sim 8$  (eq. [12]) and 2.6 for  $z > 8.5$  (eq. [13]) at the faintest magnitude. At  $z \sim 7$ , the mock-UDF12 galaxies with  $M_{UV} < -20$  have  $\beta \simeq -1.6$ , but less luminous galaxies are distributed over  $\beta = -3.4$  to  $-1.6$ . This upper limit corresponds to the upper limit of  $A_{UV}$  in our recipe. On the other hand, the observed data are distributed over  $\beta = -3.4$  to 0. Probably this larger scatter is partly because of the observational error, while we may underestimate the scatter in the simulated galaxies because we employ a unique dust attenuation model in which we adopt the Calzetti extinction law with a single dust geometry for all simulated galaxies. The mean value  $\beta = -2.1 \pm 0.2$  for  $M_{UV} = -18$  reported by Dunlop et al. (2013) is consistent with our expectation ( $\beta = -2.4 \pm 0.3$ ) at the same magnitude. A similar relation is also found by Bouwens et al. (2013). At  $z \sim 8$  and  $z \sim 9$ , the  $\beta$  distribution of the mock-UDF12 galaxies shows a large redward scatter. This is because the Ly $\alpha$  break affects the bluer band magnitude in the formulae to estimate  $\beta$  presented above. Overall the  $\beta$  distribution of the mock-UDF12 galaxies reproduce the observations very well.

### 4.3 Star Formation Rate and Specific Star Formation Rate

The star formation rate (SFR) is very important to study how the stellar components in galaxies were build up and

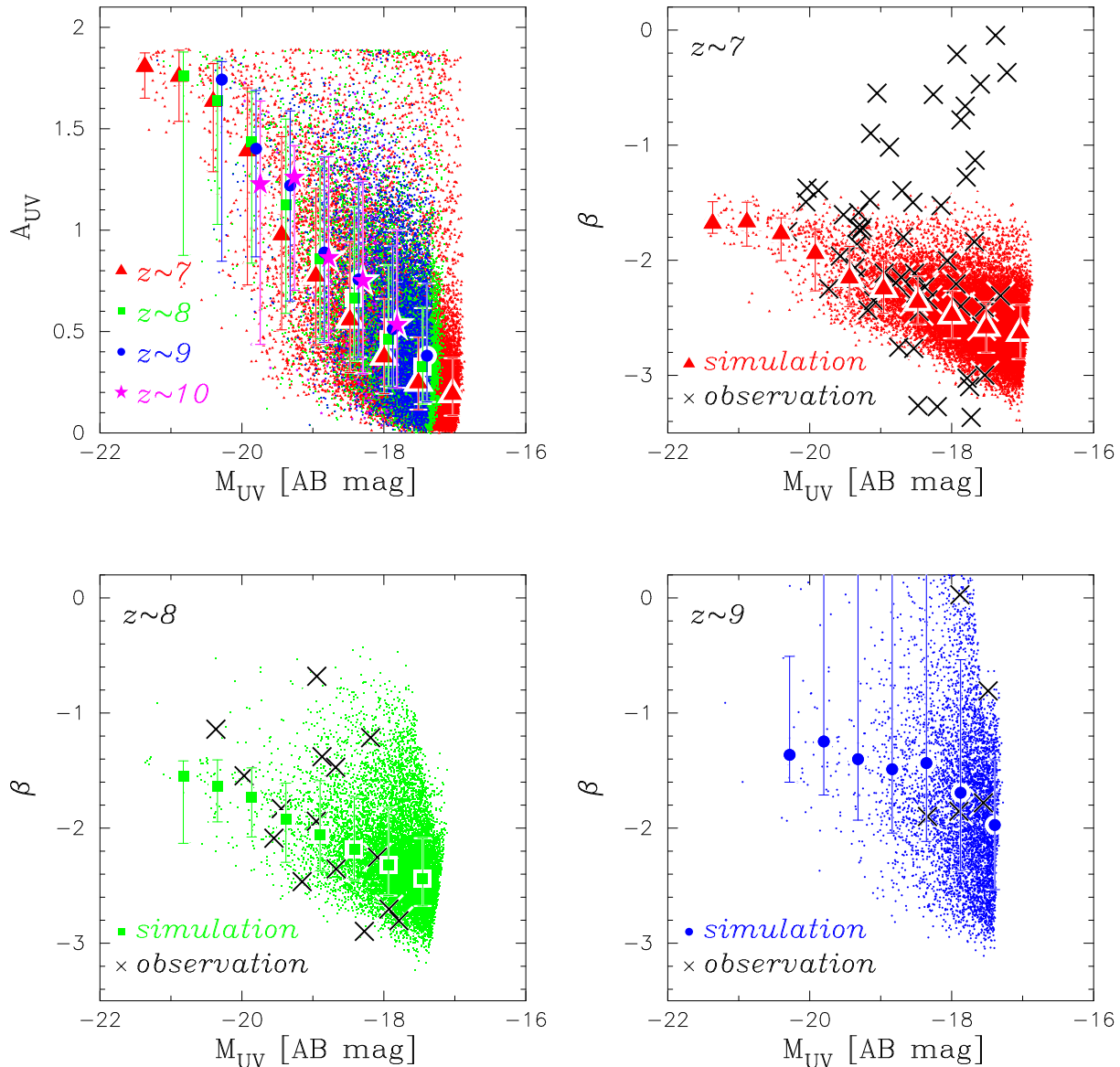


**Figure 6.** The UV dust attenuation (top left panel) and the UV slope  $\beta$  (all the rest panels) of the mock-UDF12 galaxies as a function of the absolute UV magnitude. The small points are the UV attenuation or the UV slope  $\beta$  of each simulated galaxies, while the large points with error-bars are the median values and the central 68% ranges in UV magnitude bins. We also plot the observed UV slope  $\beta$  taken from Dunlop et al. (2013) as the cross points.

how many ionizing photons were produced for the reionization of the Universe. Fig. 7 represents the SFR (left panel) and the specific SFR (sSFR; right panel) as a function of the stellar mass for the mock-UDF12 galaxies. The small symbols are the same meanings as in Fig. 5 and large symbols with error-bars are the median values and the central 68% ranges in stellar mass bins. The mock-UDF12 galaxies show an almost linear correlation between their SFR and stellar mass and form the so-called ‘main-sequence’ for star-forming galaxies (e.g., Brinchmann et al. 2004; Noeske et al. 2007; Daddi et al. 2007). In the left panel of Figure 7, the correlations at different redshifts are roughly overlapped each other, while a weak evolution of SFRs from  $z \sim 10$  to  $z \sim 7$  can be seen. This evolution is more clearly seen in the right panel showing sSFRs: higher sSFRs as higher- $z$ . This is probably because objects collapsed at higher- $z$  have

generally more dense gas, thus the SFR becomes higher in such objects. On the other hand, the dispersions in sSFRs of the different redshifts are in fact similar to each other as found from the 68% ranges shown. The apparent wider distributions for the lower- $z$  samples is just because of a larger number of the galaxies.

The sSFRs of the mock-UDF12 galaxies are higher than those of ‘main sequence’ galaxies at  $z < 2$  (Brinchmann et al. 2004; Noeske et al. 2007; Daddi et al. 2007) but are similar to those of LBGs at  $z \sim 4$  (Bouwens et al. 2012c) as shown by the dashed lines in Fig. 7. This indicates that the UDF12 galaxies at  $z > 7$  are in a similar starburst phase found in LBGs at  $z \sim 4$  rather in the normal quiescent phase found at low- $z$ . However, we find that most of our mock-UDF12 galaxies lie in the lower part than the  $z \sim 4$  observed relations.



Let us explore the physical process controlling such relations (i.e., ‘main sequence’) for the UDF12 galaxies. Suppose that the SFR is proportional to the dark matter (DM) accretion rate estimated by McBride et al. (2009); Ishiyama et al. (2013):

$$SFR = f_* \left( \frac{\Omega_B}{\Omega_M} \right) \frac{dM_{\text{halo}}}{dt}, \quad (14)$$

$$\frac{dM_{\text{halo}}}{dt} = 1.79 \times 10^{-14} f(z) \left( \frac{M_{\text{halo}}}{M_\odot} \right)^{1.094}, \quad (15)$$

and

$$f(z) = (1 + 1.75z) \sqrt{\Omega_M(1+z)^3 + \Omega_\Lambda}, \quad (16)$$

where  $f_*$  is the star formation efficiency. If we introduce a constant efficiency as  $M_*/M_{\text{halo}} \sim f_* \Omega_B / \Omega_M \sim 0.01$ , then we obtain

$$SFR(M_*) \sim (4.3_{z \sim 7}, 9.7_{z \sim 10}) \times 10^{-10} \left( \frac{M_*}{M_\odot} \right)^{1.094} M_\odot \text{ yr}^{-1}, \quad (17)$$

which is shown as the shaded area in the left panel of Fig. 7. The redshift dependence of eq. (15) from  $z \sim 7$  to  $z \sim 10$  is as small as our simulation results. We also obtain

$$sSFR(M_*) \sim (0.43_{z \sim 7}, 0.97_{z \sim 10}) \left( \frac{M_*}{M_\odot} \right)^{0.094} \text{ Gyr}^{-1}, \quad (18)$$

which is the shaded area in the left panel of Fig. 7. We find a very good agreement between our simulation and the simple estimation by equations (17) and (18) at the massive end of the stellar mass, but a small difference can be seen. This implies that  $M_*/M_{\text{halo}} \sim f_* \Omega_B / \Omega_M$  has a weak stellar (halo) mass dependence and the baryon physics is also necessary to explain the trend.

#### 4.4 Star Formation Rate Density

The star formation rate density (SFRD) is also useful to check the calibration of our simulation as well as the stellar mass function and the UV LFs. Fig. 8 shows the evolution of the SFRD from  $z \sim 10$  to  $z \sim 7$ . The triangles represent observational estimates based on galaxies with  $M_{\text{UV}} < -17.7$  (Bouwens et al. 2007, 2012a,b; Coe et al. 2013; Ellis et al. 2013; Zheng et al. 2012; Oesch et al. 2013). The all observational data are corrected for dust attenuation. Thus, the simulated data do not include any dust attenuation. The circle and square points are the SFRD of the galaxies with  $M_{\text{UV}} < -17.7$  as the observations and the total SFRD in our simulation, respectively. Our results for  $M_{\text{UV}} < -17.7$  reasonably agree with the observations within the errors, suggesting that our calibration is good enough. One important finding from the comparison is that the SFRD of the galaxies with  $M_{\text{UV}} < -17.7$  is only a minor part of the total SFRD even at  $z \sim 7$ . Therefore, we still miss a major part of the SFRD even in the current deepest survey.

#### 4.5 Mass Weighted Age

We compute the mass weighted age  $\tau_{\text{age}}$  of each mock-UDF12 galaxy to characterize the stellar population. The definition of the age is given by the following equation:

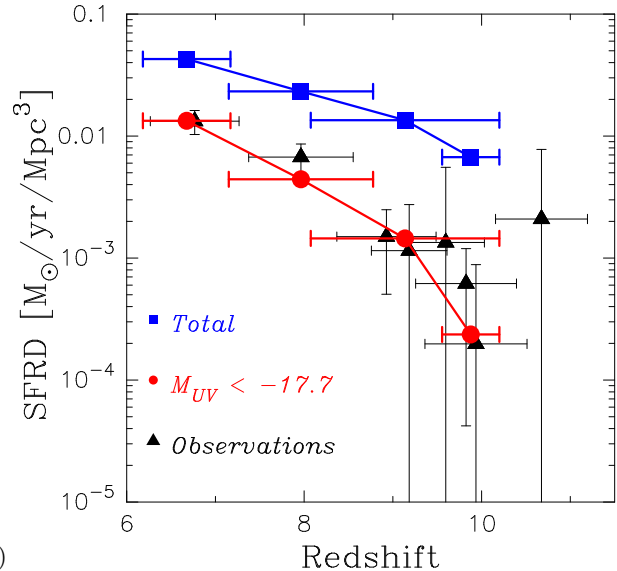


**Figure 8.** The evolution of the star formation rate density (SFRD) from  $z \sim 10$  to  $z \sim 7$ . The circle and square points are the SFRD integrated over  $M_{\text{UV}} < -17.7$  and the total SFRD in our simulation, respectively. The horizontal error-bars represent the redshift coverage of the corresponding color selection criteria. The triangles represent observational estimates with  $M_{\text{UV}} < -17.7$  (Bouwens et al. 2007, 2012a,b; Coe et al. 2013; Ellis et al. 2013; Zheng et al. 2012; Oesch et al. 2013).

$$\tau_{\text{age}} = \frac{\sum_i t_i^{\text{age}} m_i^{\text{star}}}{\sum_i m_i^{\text{star}}}, \quad (19)$$

where  $t_i^{\text{age}}$  and  $m_i^{\text{star}}$  are the age and mass of the  $i$ th star cluster in a simulated galaxy. Fig. 9 shows the mass weighted age of the mock-UDF12 galaxies as a function of their halo mass. The symbols are the same as Fig. 5. The typical ages of the mock-UDF12 galaxies are 180 Myr ( $z \sim 7$ ), 100 Myr ( $z \sim 8$ ), 80 Myr ( $z \sim 9$ ) and 50 Myr ( $z \sim 10$ ), respectively. The ages decrease with increasing redshift. On the other hand, there is a large dispersion found at halo masses less than about  $10^{10} M_\odot$ . This is because the SN feedback effectively works in such smaller mass galaxies and then the star formation occurs stochastically in such galaxies (see also the next subsection). Similar discussion can be seen in Jaacks et al. (2012b). In addition, the mass resolution of our simulation may not be enough to resolve such smaller mass galaxies and may enlarge the dispersion.

#### 4.6 Star Formation History

One has to assume a star formation history to perform the SED fitting method which is often used to explore the physical properties such as the stellar mass and the SFR of high- $z$  galaxies. A constant SFR or exponentially decreasing SFR are usually assumed. However, recent studies suggest an increasing SFR with time for high- $z$  galaxies (e.g., Reddy et al. 2012). Thus, it is very important to examine the SFH from theoretical point of view. Fig. 10 represents average SFHs of the mock-UDF12 galaxies for a certain mass range and a redshift. The lines in each panel at  $z \sim 7$  and  $z \sim 8$  show the SFHs of simulated galaxies within the stellar mass range of  $10^{10}$ – $10^{11} M_\odot$ ,  $10^9$ – $10^{10} M_\odot$ ,  $10^8$ – $10^9 M_\odot$

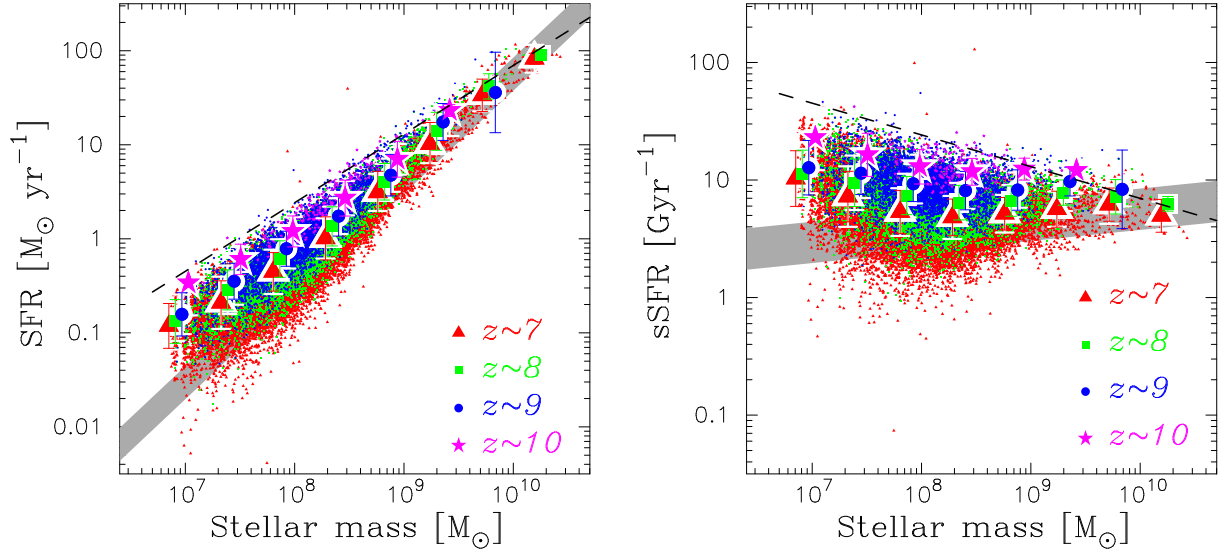


**Figure 7.** The star formation rate (left panel) and the specific star formation rate (right panel) as a function of the stellar mass for the mock-UDF12 galaxies. The small points are the SFR and sSFR of each simulated galaxy, while the large points with error-bars are the median values and the central 68% ranges in stellar mass bins. The meanings of the symbols are denoted in the panels and same as in Fig. 5. The shaded region is our simple models that the star formation rate is determined by the halo accretion rate from  $z \sim 7$  to  $z \sim 10$ . The dashed lines represent the relations between the SFR or sSFR and the stellar mass observed in the LBGs at  $z \sim 4$  (Bouwens et al. 2012c).

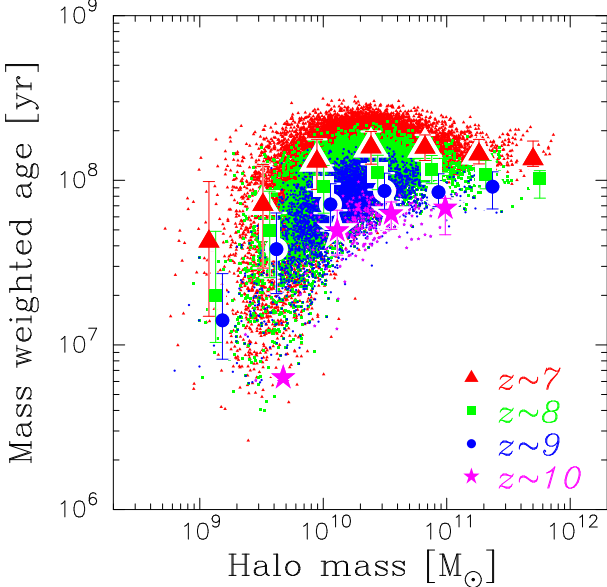


**Figure 9.** The mass weighted age of the mock-UDF12 galaxies as a function of their host halo mass. The symbols are the same as in Fig. 5.

and  $10^7$ – $10^8 M_\odot$  from the top to the bottom. The lines at  $z \sim 9$  and  $z \sim 10$  show the SFHs within the range of  $10^9$ – $10^{10} M_\odot$ ,  $10^8$ – $10^9 M_\odot$  and  $10^7$ – $10^8 M_\odot$  from the top to the bottom. The time resolution of the SFHs is set to be  $10^6$  yr to see the stochastic star formation activity. As found in Fig. 10, the SFR clearly increases with time. This suggests that it is strongly preferable to choose increasing SFR with the time (e.g., exponentially increasing) for the SED fitting method. This result is consistent with previous theoretical work (Jaacks et al. 2012b; Dayal et al. 2013). In order to ex-

amine the typical time-scale of the star formation, we adopt an exponential function:

$$SFR(t) = a \exp\left(-\frac{t}{\tau_{\text{SF}}}\right), \quad (20)$$

where  $a$  and  $\tau_{\text{SF}}$  are the normalization parameter and the typical star formation time-scale, respectively. We obtain these values with a  $\chi^2$  method. The typical star formation time-scales  $\tau_{\text{SF}}$  obtained are 250 Myr ( $z \sim 7$ ), 180 Myr ( $z \sim 8$ ), 100 Myr ( $z \sim 9$ ) and 50 Myr ( $z \sim 10$ ). These values are almost constant among different mass ranges if the redshift is the same and are somewhat longer than but still similar to the mass weighted age obtained in the previous subsection.

#### 4.7 Metallicity

Observationally, the metallicity of galaxies is determined by measuring a ratio (or ratios) of emission or absorption lines. Emission lines are usually emit from the HII regions and the photo-dissociation regions (PDRs). Thus, these lines come from the star forming region which is relatively dense region in a galaxy. In order to compare such observations with our model properly, we need to calculate the metallicity in star forming regions in a simulated galaxy rather than that in the whole of the galaxy. We here introduce a new definition of the metallicity for simulated galaxies as following equation:

$$Z_{\text{neb}} = \frac{\sum_i Z_i L_i^{\text{LyC}}}{\sum_i L_i^{\text{LyC}}}, \quad (21)$$

where  $Z_i$  and  $L_i^{\text{LyC}}$  are the metallicity and the intrinsic Lyman continuum luminosity of  $i$ th star particle in a simulated galaxy. We have assumed that the gas metallicity around a star particle is the same as that of the star particle. In this definition, only the metal around the very young star particles is taken into account and the metal around aged star

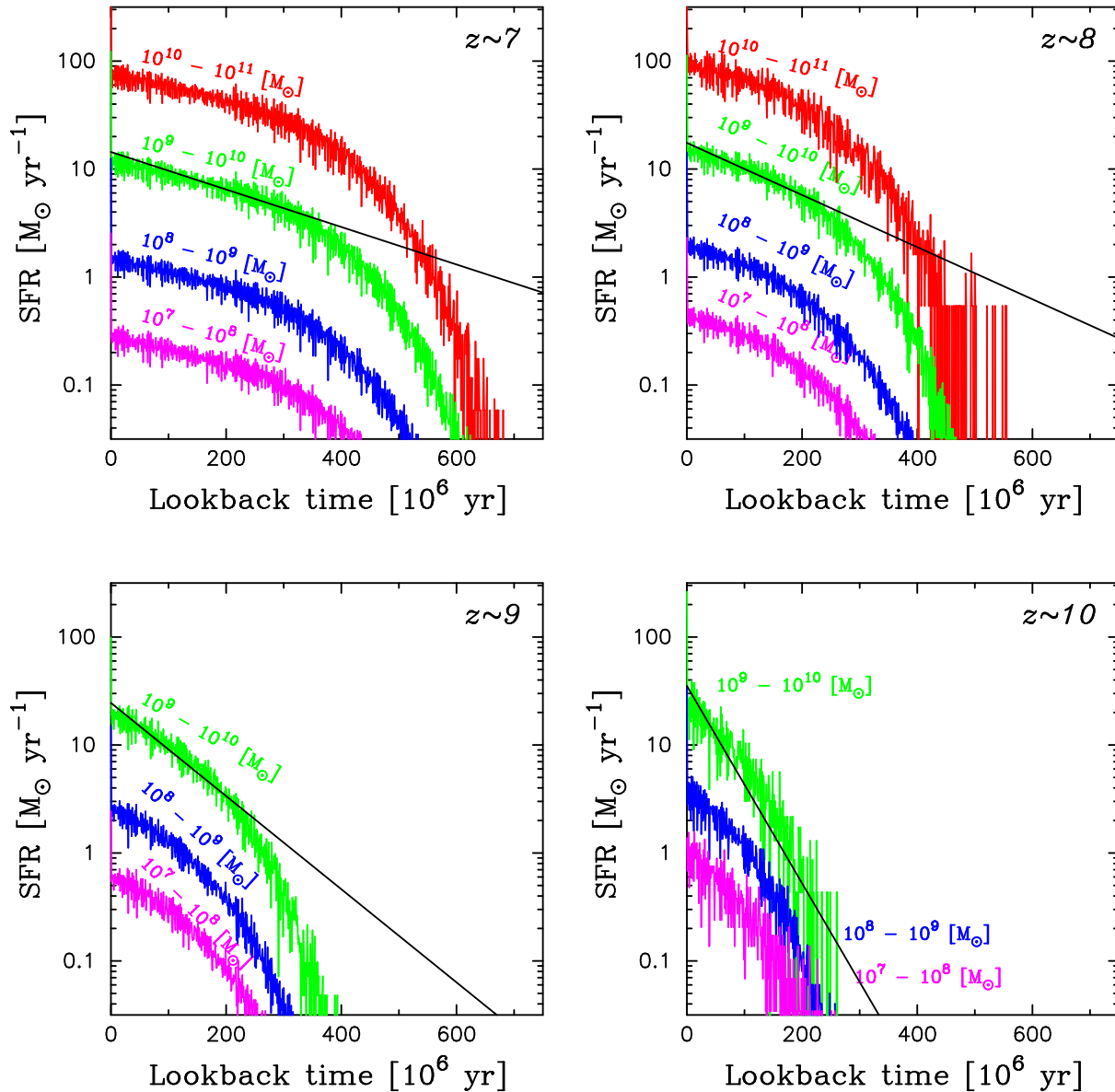


**Figure 10.** The average star formation history of the mock-UDF12 galaxies within a certain mass range. The lines in each panel at  $z \sim 7$  and  $z \sim 8$  show the SHFs of simulated galaxies within the stellar mass range of  $10^{10}$ – $10^{11} M_{\odot}$ ,  $10^9$ – $10^{10} M_{\odot}$ ,  $10^8$ – $10^9 M_{\odot}$  and  $10^7$ – $10^8 M_{\odot}$  from the top to the bottom. The lines at  $z \sim 9$  and  $z \sim 10$  show the SHFs within the range of  $10^9$ – $10^{10} M_{\odot}$ ,  $10^8$ – $10^9 M_{\odot}$  and  $10^7$ – $10^8 M_{\odot}$  from the top to the bottom. The time bin of this calculation is  $10^6$  yr. The solid lines of each panel is an exponential fitting.

particles and the metal far from star forming regions do not contribute to the metallicity. The metallicity of this definition is usually higher than that averaged over the whole of a simulated galaxy. We call this metallicity the nebular metallicity.

Fig. 11 represents the nebular metallicity of the mock-UDF12 galaxies as a function of their host halo mass. The symbols are the same as Fig. 5. The nebular metallicity is roughly proportional to their host halo mass although the dispersion is large. We also find that the metallicity evolution from  $z \sim 10$  to  $z \sim 7$  is weak as with the SFR. Interestingly, the metallicity of some galaxies reaches at  $> 0.1$  solar metallicity ( $Z_{\odot} = 0.02$ ) even at  $z \sim 10$ . These suggest that the metal enrichment is a rapid process.

#### 4.8 Morphology and Size

In order to explore the size and the morphology of the mock-UDF12 galaxies, it is necessary to resolve the inner structure of the simulated galaxies. Thus, we discuss only massive (UV bright:  $M_{UV} < -20$ ) galaxies which are composed of at least about 1,000 star particles. Fig. 12 shows the surface brightness distributions at the rest-frame 1500 Å of the UV brightest galaxy among the mock-UDF12 galaxies at  $z \sim 7$  (the left panel) and  $z \sim 8$  (the right panel), respectively. We have applied a Gaussian smoothing with  $\sigma_G = 0.1''$  in order to take the point-spread-function of the HST/WFC3 approximately into account. The images of the UV brightest mock-UDF12 galaxies are roughly round but still show somewhat clumpy and elongated structure, in particular in the  $z \sim 7$

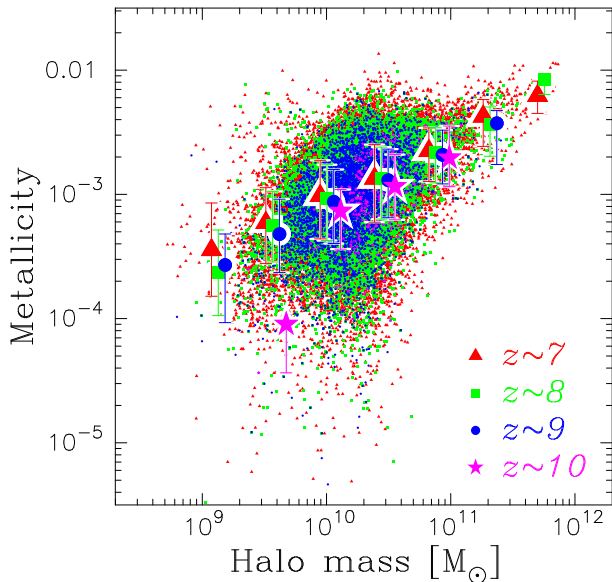


**Figure 11.** The nebular metallicity of the mock-UDF12 galaxies as a function of their halo mass. The symbols are the same as Fig. 5.

case. Interestingly, such a shape has been found in the observational data (Ono et al. 2013). To compare with observational studies (the brightness profile), we make a stacked UV images of the mock-UDF12 galaxies. To do so, we stack the distributions of star particles projected on the sky using the light-cone output of the mock-UDF12 galaxies. In the stacking process, we regard the luminosity center of each galaxy as the galaxy center and we do not choose any specific direction of the galaxy (i.e., the position angles in the stacking are random). The spatial unit of the galaxies is the physical unit not comoving unit. In our simulation box, the numbers of galaxies with  $M_{UV} < -21$  and  $-21 < M_{UV} < -20$  are 32 (6) and 155 (45) at  $z \sim 7$  ( $z \sim 8$ ), respectively. Fig. 13 shows the azimuthally summed up and normalized cumulative profiles of the stacked images of the simulated galaxies at  $z \sim 7$  (left panel) and  $z \sim 8$  (right panel). The solid and dashed lines represent the profiles for  $M_{UV} < -21$  and  $-21 < M_{UV} < -20$ , respectively. The half light radii of the stacked images with  $M_{UV} < -21$  ( $-21 < M_{UV} < -20$ ) are 0.60 kpc (0.55 kpc) at  $z \sim 7$  and 0.48 kpc (0.55 kpc) at  $z \sim 8$ , respectively. These results are also similar to the results of the UDF12 campaign (Ono et al. 2013).

## 5 DISCUSSION

We have presented some physical properties of the UDF12 galaxies at  $z \sim 7$ –10 expected from our cosmological hydrodynamic simulation. Here we discuss a few additional issues derived from the simulation.

### 5.1 $z > 10$ Galaxies

So far, we have studied only upto  $z \sim 10$  selected galaxies. Oesch et al. (2013) (see also Bouwens et al. 2011; Ellis et al. 2013) presented one  $z = 11.8$  galaxy candidate (XDFjh-39546284). Thus, it is also interesting to study the physical

properties of such  $z > 10$  galaxies not only for HST deep survey but also for future observations with the James Webb Space Telescope and 30 m telescopes. Here, we use the same color selection criterion as Oesch et al. (2013):

$$JH_{140} - H_{160} > 1.0. \quad (22)$$

Moreover, we adopt the detection limit criterion of  $H_{160} < 30$ . As a result, we find 81 simulated galaxies from  $z = 10.6$  to  $z = 11.7$  in our simulation box. All their  $H_{160}$  band magnitudes are fainter than 28.6. We note that our field-of-view (FOV) is about 400 arcmin<sup>2</sup> at the redshift and then the expected number is about two galaxies per one FOV of the UDF12 survey. Therefore, the detection of one such highest- $z$  galaxy in the UDF12 campaign is consistent with our simulation if we consider the Poisson error. The halo and stellar masses of these galaxies are  $5 \times 10^9 - 1 \times 10^{11} M_{\odot}$  and  $2 \times 10^7 - 2 \times 10^9 M_{\odot}$ , respectively. The stellar mass weighted age and the nebular metallicity  $Z_{\text{neb}}$  are  $1 \times 10^7 - 8 \times 10^7$  yr and 0.00005 – 0.003, respectively. Clearly,  $z > 10$  galaxies selected by the drop-out technique are very early evolutionary phase objects.

### 5.2 Prediction for ALMA

As discussed in section 4.2, the mock-UDF12 galaxies suffer a modest amount of dust attenuation. Therefore, these galaxies also emit the thermal radiation from dust in the far-infrared wavelength. They could be detectable with the Atacama Large Millimetre-submillimetre Array (ALMA). Submm observations of very high- $z$  galaxies is also important to know the chemical enrichment and the dust formation at very high- $z$ . According to Shimizu, Yoshida & Okamoto (2012), the submm flux of star-forming galaxies with  $\text{SFR} \sim 100 M_{\odot}/\text{yr}$  is about 1 mJy. Indeed, some of our simulated galaxies have  $\text{SFR} \sim 100 M_{\odot}/\text{yr}$  and the galaxies would be detectable with ALMA. We calculate the submm flux of the simulated galaxies by the same procedure as Shimizu, Yoshida & Okamoto (2012).

The dust temperature for our sample galaxies is typically  $\sim 30$  K. Fig. 14 shows the expected submm flux density at 350 GHz in the observer’s frame as a function of the observed  $H_{160}$  band magnitude. We find a tight correlation between the two quantities independent of the redshift. If we set the detection limit as 0.1 mJy, galaxies brighter than  $H_{160} = 27.5$  may be detected. However, most of the galaxies with  $H_{160} = 27.5$  actually have much fainter submm flux density. In order to increase the probability of the detection, we should observe galaxies with  $H_{160} > 27$  or even 26.5. Actually, the brightest  $H_{160}$  magnitude in the UDF12 survey is  $H_{160} = 27.2$ . However, other wide-field surveys like the Brightest of Reionizing Galaxies (BoRG) survey (Trenti et al. 2011, 2012; Bradley et al. 2012) and surveys for gravitationally-lensed galaxies like the Cluster Lensing And Supernova survey with Hubble (CLASH) survey (Postman et al. 2012) have reported detection of some galaxies with  $H_{160} < 27$  at  $z > 7$ . These galaxies would be good targets for ALMA.

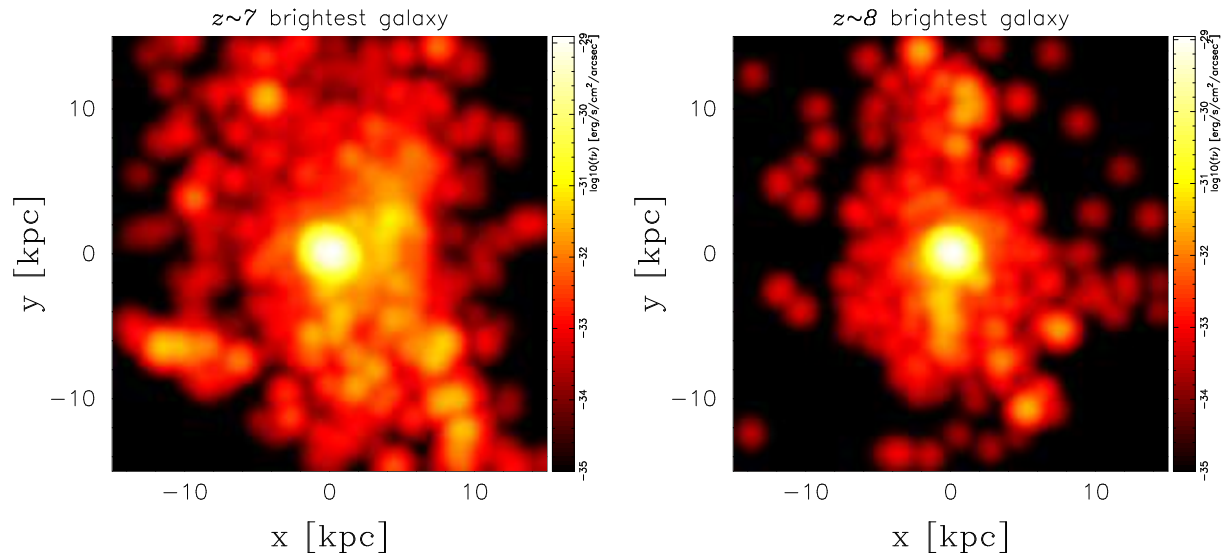


**Figure 12.** The surface brightness distributions at the rest-frame  $1500 \text{ \AA}$  of the UV brightest galaxy among the mock-UDF12 galaxies at  $z \sim 7$  (the left panel) and  $z \sim 8$  (the right panel), respectively.

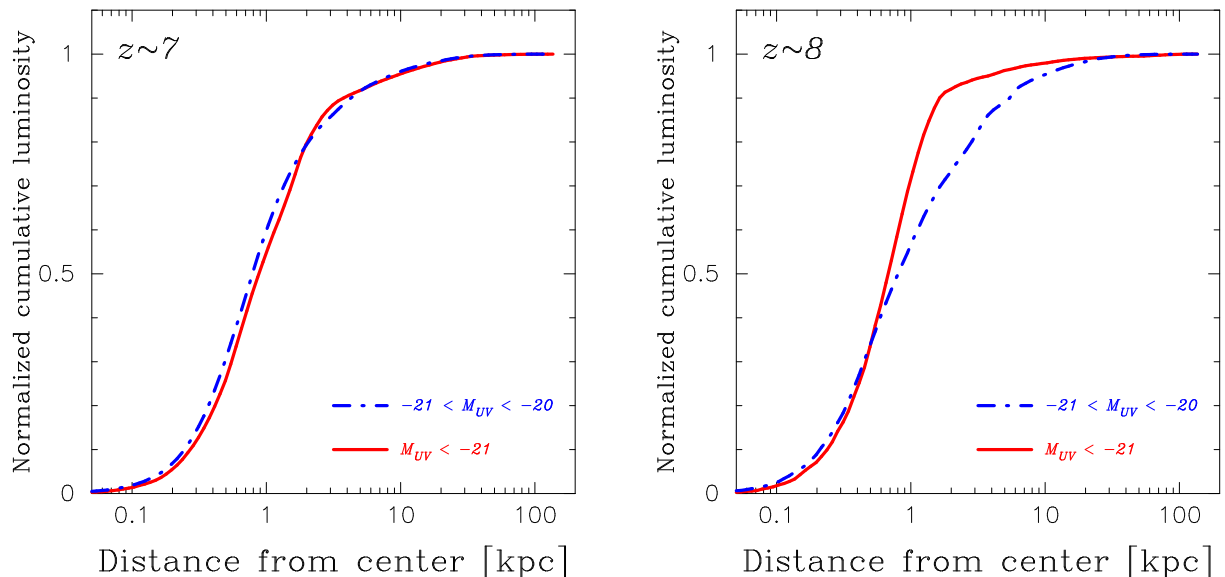


**Figure 13.** The azimuthally summed up and normalized cumulative profiles with two  $M_{UV}$  ranges at  $z \sim 7$  (the left panel) and  $z \sim 8$  (the right panel). The solid and dashed lines are the profiles of the stacked images with  $M_{UV} < -21$  and  $-21 < M_{UV} < -20$ , respectively.

### 5.3 Galaxies selected and not selected by the UDF12 Survey

So far we have discussed the galaxies detected and color-selected by the UDF12 campaign. As shown in Fig. 4, however, most of the simulated galaxies are not selected owing to either detection limit or the color criteria. Indeed, the number fraction of the selected galaxies is about 12% for  $z \sim 7$  and about 2% for  $z \sim 10$ . What about the corresponding fraction in terms of the cosmic star formation density (SFRD)? Fig. 8 shows the evolution of the SFRD from  $z \sim 10$  to  $z \sim 7$ . There, we consider an additional condition of  $M_{UV} < -17.7$  in order to directly compare our simulation with the observations. This condition is about one magnitude brighter than the detection limit of the UDF12

campaign. In this subsection, we measure the contribution of the UDF12 galaxies to the cosmic SFRD quantitatively. We find that the contributions to the total SFRD of the mock-UDF12 galaxies are 52%, 39%, 30% and 12% for  $z \sim 7, 8, 9$  and  $z \sim 10$ , respectively. This means that we do not see faint galaxies which contributed to the dominant part of the SFRD. Note that we can resolve only halos with  $> 10^9 M_\odot$  in our simulation. Thus, the relative contribution of the detectable galaxies could be even smaller if there are a significant amount of less massive galaxies than our simulation.

Let us study the properties of galaxies unselected by the UDF12 survey. There are four cases: (1) galaxies satisfy the color selection criteria and are bright enough to be detected, (2) galaxies satisfy the color selection criteria but are too faint to be detected, (3) galaxies do not satisfy the color

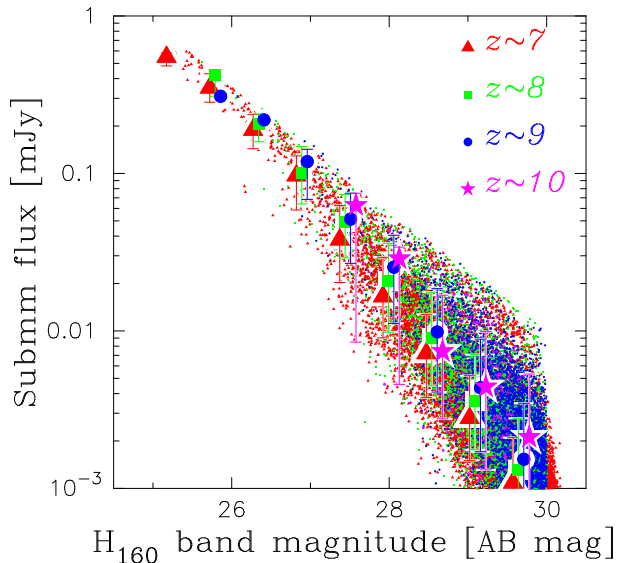


**Figure 14.** The expected submm flux density at 350 GHz in the observer’s frame of the mock-UDF12 galaxies as a function of the observed  $H_{160}$  band magnitude. The symbols are the same as Fig. 5.

criteria but are bright enough to be detected and (4) galaxies do not satisfy neither color criteria nor the brightness limit. Table 1 represents the contributions of each case to the SFRD. We find that the simulated galaxies satisfying the color criteria (cases [1] and [2]) contribute to a major fraction of the SFRD (85–95%) but most of it comes from galaxies fainter than the current detection limit (i.e., case [2]), except at  $z = 7$  where the detected and not-detected galaxies have similar contributions. Many of these faint galaxies in the case (2) will be detected by the next generation telescopes. On the other hand, the simulated galaxies of the cases (3) and (4) contribute to only a minor fraction of the SFRD (5–15%). Interestingly, all these galaxies reside around the redshift boundaries defined by the color selection and there are no galaxies around middle of the redshift ranges. The deviation from color selection criteria of the cases (3) and (4) galaxies is less than 0.4 mag. Thus, if the selection criteria are somewhat relaxed, the galaxies bright enough (i.e., case [3]) can be selected by the color selection. In other words, there are no galaxies with very red UV colors at  $z \sim 7, 8, 9$  and  $z \sim 10$  in our simulation.

Finally, we provide a prediction after the James Webb Space Telescope (JWST) starts operation. The values in parentheses of Table 1 represent the star formation contribution of each case with the detection limit of  $< 32$  which corresponds to the JWST one. We find that the JWST can detect more than half (72–77%) of star formation activity. Yet, much fainter galaxies accounting for  $\sim 28\%$  of the  $z \sim 10$  star forming activity will still remain undetectable even with the JWST.

## 6 CONCLUSION

We have made a cosmological hydrodynamic simulation tailored to examine the physical properties of very high- $z$  galaxies detected by the deep survey with

HST/WFC3 performed in 2012, the so-called UDF12 campaign (Ellis et al. 2013; McLure et al. 2013; Schenker et al. 2013; Dunlop et al. 2013; Robertson et al. 2013; Ono et al. 2013; Koekemoer et al. 2013; Oesch et al. 2013). Our simulation code follows the formation and the evolution of star forming galaxies by new feedback models based on Okamoto et al. (2010) and can reproduce the statistical properties of star forming galaxies such as Lyman break galaxies (LBGs), Lyman  $\alpha$  emitters and sub-mm galaxies (Shimizu, Yoshida & Okamoto 2011, 2012). First, we calibrate our model parameters so as to reproduce not only the stellar mass function at  $z \sim 7$  but also the UV luminosity function from  $z \sim 7$  to  $z \sim 10$ . Then, we generate a light-cone output which extends from  $z = 6$  to  $z = 12$  using a number of simulation outputs in order to directly compare our model with the observations. It is the most important point of this study that we adopt the same color selection criteria as the UDF12 campaign to select galaxies from our simulation. We call the selected galaxies the mock-UDF12 galaxies. Using these simulated galaxies as a proxy of the observed UDF12 galaxies, we can examine the physical properties such as the halo and stellar masses, the specific star formation rate, the star formation history, etc. of the real galaxies. This is a new approach to reveal the physical properties of the highest- $z$  galaxies for which the so-called SED fitting method may not be reliable because we have few photometric data points only in the rest-frame UV.

We find that the observed UV luminosity of the mock-UDF12 galaxies is almost linearly proportional to their host halo mass and the correlation does not change so much along the redshift from  $z \sim 7$  to  $z \sim 10$ . For example, the halo mass at  $M_{UV} = -21$  is about  $4 \times 10^{11} M_{\odot}$ . The stellar mass of the galaxies is also proportional to the UV luminosity but the power-law slope is about 1.4. We have derived the fitting formulae for the halo and stellar masses as a function of the UV absolute magnitude not corrected for the dust attenuation. We also find that many mock-UDF12 galaxies are affected by the dust attenuation. The amount of the attenuation well correlates with the UV magnitude but shows a large dispersion ranging from  $A_{UV} = 0$  to 1.9 (or  $A_V = 0$  to 0.76) which is larger than that argued by Dunlop et al. (2013). Nevertheless, our simulation reproduces the observed UV slope  $\beta$  distribution reported by Dunlop et al. (2013). The mean UV slope also correlates with the UV magnitude. Such a trend consistent with the observational results (Bouwens et al. 2013). There is no luminous ( $M_{UV} < -21$ ) and less attenuation ( $A_{UV} < 1.5$ ) galaxies in our simulation.

The star formation rate (SFR) is proportional to the stellar mass with a power-law slope about unity. The specific star formation rate (sSFR) shows a very weak dependency on the stellar mass and the value is about  $10 \text{ Gyr}^{-1}$  which is higher than that of the main-sequence for star-forming galaxies at  $z < 2$  (e.g., Brinchmann et al. 2004; Noeske et al. 2007; Daddi et al. 2007) but is similar to that of LBGs at  $z > 4$  (e.g., Bouwens et al. 2012c). This indicates that LBGs from  $z \sim 4$  to  $z \sim 10$  are in a similar starburst phase. With the hypothesis of the SFR proportional to the dark matter accretion rate, these relations between the stellar mass and the SFR or the sSFR are reproduced reasonably well. This supports the hypothesis. However, the slight

fraction	redshift	case (1)	case (2)	case (3)	case (4)
$P_{\text{SFRD}}$	$z \sim 7$	0.517 (0.774)	0.347 (0.089)	0.086 (0.122)	0.051 (0.015)
	$z \sim 8$	0.388 (0.749)	0.460 (0.098)	0.071 (0.138)	0.081 (0.015)
	$z \sim 9$	0.295 (0.793)	0.646 (0.149)	0.019 (0.055)	0.039 (0.003)
	$z \sim 10$	0.122 (0.723)	0.825 (0.224)	0.008 (0.047)	0.045 (0.006)

**Table 1.** The fraction in the star formation rate density ( $P_{\text{SFRD}}$ ) of the following four cases: (1) galaxies satisfy the color selection criteria and are bright enough to be detected, (2) galaxies satisfy the color selection criteria but are too faint to be detected, (3) galaxies do not satisfy the color criteria but are bright enough to be detected, and (4) galaxies do not satisfy neither color criteria nor the brightness limit. The values without and with parentheses are the fractions for the detection limits of  $< 30$  and  $< 32$ , respectively.

gap between our model and the simple model means that the baryon physics is also necessary to reproduce the trend. The evolution of the cosmic SFR density from  $z \sim 7$  to  $z \sim 10$  in our simulation reasonably matches with the recent observed results (Bouwens et al. 2007, 2012a,b; Coe et al. 2013; Ellis et al. 2013; Zheng et al. 2012; Oesch et al. 2013).

We have also examined the star formation history (SFH) of the mock-UDF12 galaxies and found an increasing SFR with time. This trend is independent of the redshift and the mass. Such an increasing SFH is also suggested by recent observational studies (e.g., Reddy et al. 2012). Therefore we conclude that an increasing SFH should be assumed in the SED fitting work where usually a constant or decreasing SFH has been assumed so far. If we fit the increasing SFH by an exponential function, the typical time-scales for  $z \sim 7$ , 8, 9 and  $z \sim 10$  galaxies are 250 Myr, 180 Myr, 100 Myr and 50 Myr, respectively. We also find that the mass-weighted average ages of the mock-UDF12 galaxies are 180 Myr ( $z \sim 7$ ), 100 Myr ( $z \sim 8$ ), 80 Myr ( $z \sim 9$ ) and 50 Myr ( $z \sim 10$ ). These time-scales are roughly consistent with each other.

We have introduced an average metallicity weighted by Lyman continuum luminosity. We call it the nebular metallicity which is the one usually measured from emission line ratios observationally. Interestingly, the nebular metallicity of some mock-UDF12 galaxies is 0.1 to 0.5 solar metallicity. The result implies that the metal enrichment proceeds rapidly even at  $z \sim 10$ . We have also explored the size and morphology of the mock-UDF12 galaxies. We find that the UV brightest galaxies at  $z \sim 7$  and  $z \sim 8$  are roughly round but still show clumpiness and asymmetry. After stacking the distributions of star particles projected to the observer’s sky in the light-cone output and produced the stacked UV images for galaxies within the two brightest UV magnitude ranges, we find that the half light radii of the stacked images at  $z \sim 7$  ( $z \sim 8$ ) are 0.60 kpc (0.48 kpc) for the  $M_{\text{UV}} < -21$  cases and 0.55 kpc (0.55 kpc) for the  $-21 < M_{\text{UV}} < -20$  cases, respectively. These results are consistent with the recent observational results (Ono et al. 2013).

Finally, we have discussed a few additional issues derived from our simulation. There is one candidate galaxy at  $z = 11.8$  in the UDF (Bouwens et al. 2011; Ellis et al. 2013; Oesch et al. 2013). In our simulation, we expect two galaxies brighter than the current detection limit and satisfying the color selection for  $z > 10$  per one field-of-view of the UDF12 survey. Therefore, the number density is consistent with each other. We also present the expected submm flux density of the mock-UDF12 galaxies. The galaxies with  $H_{160} \leq 27$ , the expected submm flux density is  $\geq 0.1$  mJy

at 350 GHz in the observer’s rest-frame. This will be detectable with the ALMA. We have examined the fraction of galaxies selected or not selected by the UDF12 survey. The detected and color-selected galaxies contribute to only 52%, 39%, 30% and 12% of the cosmic star formation rate density (SFRD) at  $z \sim 7$ , 8, 9 and  $z \sim 10$ , respectively. A significant part (35–83%) of the SFRD comes from galaxies satisfying the color selection criteria but not bright enough to be detected with the current detection limit. If we lower the detection limit of  $< 32$  which corresponds to that of the JWST, the fraction of the detected and color-selected galaxies would drastically increases to 77%, 75%, 79% and 72% at  $z \sim 7$ , 8, 9 and  $z \sim 10$ , respectively. Yet, 28% star forming activity at  $z \sim 10$  remains undetectable even with the JWST. The fraction of the galaxies not satisfying the color criteria is as small as 5–14% and they reside around not far from the color boundary. Therefore, we conclude that no galaxy with a very red UV color exists at  $z > 7$  in our simulation.

## ACKNOWLEDGMENTS

We thank an anonymous referee for her/his constructive comments. We also thank Tomoaki Ishiyama for his comments on the halo accretion rate of galaxies. Numerical simulations have been performed with the EUP, PRIMO and SGI cluster system installed at the Institute for the Physics and Mathematics of the Universe, University of Tokyo and with T2K Tsukuba at Centre for Computational Sciences in University of Tsukuba. IS and AKI acknowledge the financial support of Grant-in-Aid for Young Scientists (A: 23684010) by MEXT, Japan. This work is partially supported by Grant-in-Aid for Young Scientists (S) (20674003) and by the FIRST program Subaru Measurements of Images and Redshifts (SuMIRe) by the Council for Science and Technology Policy. TO acknowledges the financial support of Grant-in-Aid for Young Scientists (B: 24740112).

## REFERENCES

- Behroozi, P. S., Wechsler, R. H., Conroy, C., 2013, ApJ, 770, 57
- Biffi, V., Maio, U., 2013, MNRAS, 436, 1621
- Bouwens, R. J., et al., 2004, ApJ, 616, L79
- Bouwens, R. J., Illingworth, G. D., Franx, M., Ford, H., 2007, ApJ, 670, 928
- Bouwens, R. J., et al., 2010, ApJ, 709, L133
- Bouwens, R. J., et al., 2011, ApJ, 737, 90

- Bouwens, R. J., et al., 2011, *Nature*, 469, 504  
 Bouwens, R. J., et al., 2012a, arXiv:1211.2230  
 Bouwens, R. J., et al., 2012b, *ApJ*, 752, L5  
 Bouwens, R. J., et al., 2012c, *ApJ*, 754, 83  
 Bouwens, R. J., et al., 2013, arXiv:1306.2950  
 Bowler, R. A. A., et al., 2012, *MNRAS*, 426, 2772  
 Bradley, L. D., et al., 2012, *ApJ*, 760, 108  
 Brammer, G. B., et al., 2013, *ApJ*, 765, L2  
 Brinchmann, J., Charlot, S., White, S. D. M., Tremonti, C., Kauffmann, G., Heckman, T., Brinkmann, J., 2004, *MNRAS*, 351, 1151  
 Bunker, A. J., et al., 2013, *MNRAS*, 430, 3314  
 Calzetti, D., Armus L., Bohlin, R. C., Kinney, A. L., Koornneef, J., Storchi-Bergmann, T., 2000, *ApJ*, 533, 682  
 Capak, P. L., Faisst, A., Vieira, J. D., Tacchella, S., Carollo, M., Scoville, N. Z., 2013, *ApJ*, 773, 14  
 Castellano, M., et al., 2010b, *A&A*, 524, A28  
 Coe, D., et al., 2013, *ApJ*, 762, 32  
 Daddi, E., et al., 2007, *ApJ*, 670, 156  
 Dayal, P., Dunlop, J. S., Maio, U., Ciardi, B., 2013, *MNRAS*, 434, 1486  
 Draine, B. T., Lee, H. M., 1984, *ApJ*, 285, 89  
 Draine, B. T., et al., 2007, *ApJ*, 663, 866  
 Dunlop, J. S., et al., 2013, *MNRAS*, 432, 3520  
 Ellis, R. S., et al., 2013, *ApJ*, 763, L7  
 Ferland, G. J., Koristra, K. T., Verner, D. A., Ferguson, J. W., Kingdon, J. B., Verner, E. M., *PASP*, 110, 761  
 Finkelstein, S. L., et al., 2013, *Nature*, 502, 524  
 Fioc, M., Rocca-Volmerange, B., 1997, *A&A*, 326, 950  
 González, V., Labbé, I., Bouwens, R. J., Illingworth, G., Franx, M., Kriek M., 2011, *ApJ*, 735, L34  
 Jaacks, J., Thompson, R., Nagamine, K., 2013, *ApJ*, 766, 94  
 Jaacks, J., Choi, J.-H., Nagamine, K., Thompson, R., Varghese, S., 2012, *MNRAS*, 420, 1606  
 Jaacks, J., Nagamine, K., Choi, J.-H., 2012, *MNRAS*, 427, 403  
 Inoue, A. K., 2003, *PASJ*, 55, 901  
 Inoue, A. K., 2011a, *MNRAS*, 415, 2920  
 Inoue, A. K., 2011b, *Earth, Planets and Space*, 63, 1027  
 Inoue, A. K., Buat, V., Burgarella, D., Panuzzo, P., Takeuchi, T. T., Iglesias-Páramo, J., 2006, *MNRAS*, 370, 380  
 Inoue, A. K., Shimizu, I., Tamura, Y., Matsuo, H., Okamoto, T., Yoshida, N., 2014, *ApJ*, 780, 18  
 Ishiyama T., et al., 2013, *ApJ*, 767, 146  
 Kimm, T., Cen, R., 2013, *ApJ*, 776, 35  
 Koekemoer, A. M., 2013, *ApJS*, 209, 3  
 Komatsu, E., et al., 2011, *ApJS*, 192, 18  
 Labbé, I., et al., 2010, *ApJ*, 716, L103  
 McBride, J., Fakhouri, O., Ma, C.-P. 2009, *MNRAS*, 398, 1858  
 Madau, P., 1995, *ApJ*, 441, 18  
 Martin, C. L., 2005, *ApJ*, 621, 227  
 McLure, R. J., et al., 2010, *MNRAS*, 403, 960  
 McLure, R. J., et al., 2013, *MNRAS*, 432, 2696  
 Nagamine, K., Ouchi, M., Springel, V., Hernquist, L., 2010, *PASJ*, 62, 1455  
 Noeske, K. G., et al., 2007, *ApJ*, 660, L43  
 Nozawa, T., Kozasa, T., Umeda, H., Maeda, K., Nomoto, K., 2003, *ApJ*, 598, 785  
 Oesch, P. A., et al., 2010, *ApJ*, 709, L16  
 Oesch, P. A., et al., 2012, *ApJ*, 759, 135  
 Oesch, P. A., et al., 2013, *ApJ*, 773, 75  
 Okamoto, T., Eke, V. R., Frenk, C. S., Jenkins, A., 2005, *MNRAS*, 363, 1299  
 Okamoto, T., Frenk, C. S., Jenkins, A., Theuns, T. 2010, *MNRAS*, 406, 208  
 Okamoto, T., Frenk, C. S., 2009, *MNRAS*, 399, L174  
 Okamoto, T., Nemmen, R. S., Bower, R. G., 2008, *MNRAS*, 385, 161  
 Oke, J. B., 1990, *AJ*, 99, 1621  
 Ono, Y., et al., 2012, *ApJ*, 744, 83  
 Ono, Y., et al., 2013, *ApJ*, 777, 155  
 Ota, K., et al., 2008, *ApJ*, 677, 12  
 Ouchi, M., et al., 2009, *ApJ*, 706, 1136  
 Ouchi, M., et al., 2010, *ApJ*, 723, 869  
 Overzier, R., et al., 2013, *MNRAS*, 428, 778  
 Postman, M., et al., 2012, *ApJS*, 199, 25  
 Reddy, N. A., Pettini, M., Steidel, C. C., Shapley, A. E., Erb, D. K., Law, D. R., 2012, *ApJ*, 754, 25  
 Robertson, B. E., Ellis, R. S., Dunlop, J. S., McLure, R., 2010, *Nature*, 468, 49  
 Robertson, B. E., et al., 2013, *ApJ*, 768, 71  
 Salvaterra, R., Ferrara, A., Dayal, P., 2011, *MNRAS*, 414, 847  
 Salvaterra, R., Maio, U., Ciardi, B., Campisi, M. A., 2013, *MNRAS*, 429, 2718  
 Sawicki, M., Yee, H. K. C., 1998, *AJ*, 115, 1329  
 Schaerer, D., de Barros, S., 2008, *A&A*, 502, 423  
 Schenker, M. A., et al., 2013, *ApJ*, 768, 196  
 Shibuya, T., et al., 2012, *ApJ*, 752, 114  
 Shimizu, I., Yoshida, N., Okamoto, T., 2011, *MNRAS*, 418, 2273  
 Shimizu, I., Yoshida, N., Okamoto, T., 2012, *MNRAS*, 427, 2866  
 Shimizu, I., Inoue, Akio. K., 2013, *PASJ*, 65, 96  
 Springel, V., White, S. D. M., Tormen, G., Kauffmann, G., 2001, *MNRAS*, 328, 726  
 Springel, V., 2005, *MNRAS*, 364, 1105  
 Todini, P., Ferrara, A., 2001, *MNRAS*, 325, 726  
 Trenti, M., et al., 2011, *ApJ*, 727, L39  
 Trenti, M., et al., 2012, *ApJ*, 746, 55  
 Treu, T., Schmidt, K. B., Trenti, M., Bradley, L. D., Stiavelli, M., 2013, *ApJ*, 775, 29  
 Vanzella, E., et al., 2011, *ApJ*, 730, L35  
 Wilkins, S. M., et al., 2010, *MNRAS*, 403, 938  
 Xu, C., Buat, V., 1995, *A&A*, 293, L65  
 Yan, H., Windhorst, R. A., 2004, *ApJ*, 612, L93  
 Zheng, W., et al., 2012, *Nature*, 489, 406

This paper has been typeset from a  $\text{\TeX}$ / $\text{\LaTeX}$  file prepared by the author.